Modulation of the Madden-Julian Oscillation by ENSO: Inferences from Observations and GCM Simulations

Chi-Yung TAM

Atmospheric and Oceanic Sciences Program, Princeton University, Princeton, New Jersey, USA

and

Ngar-Cheung LAU

NOAA/Geophysical Fluid Dynamics Laboratory, Princeton University, Princeton, New Jersey, USA

(Manuscript received 20 January 2005, in final form 31 May 2005)

Abstract

The impact of the El Niño-Southern Oscillation (ENSO) on the Madden-Julian Oscillation (MJO) is studied, based on reanalysis data and output from an ensemble general circulation model (GCM) experiment. Observed monthly sea surface temperature variations over the period of 1950–99 are imposed in the deep tropical eastern/central Pacific in the course of the SST experiment. Both GCM, and reanalysis data, indicate that intraseasonal activity of the low-level zonal wind is enhanced (reduced) over the central (western) Pacific during El Niño events. The propagation and growth/decay characterisitcis of the MJO in different phases of ENSO is also examined, based on a lag correlation technique. During warm events there is an eastward shift in the locations of strong growth and decay, and the propagation of the MJO becomes slower in the warm ENSO phase. These changes are reversed during La Niña epsiodes.

Using output from the GCM experiment, the effects of ENSO on the circulation and convection during the MJO lifecycle are studied in detail. Further eastward penetration of MJO-related convection is simulated during warm events over the central Pacific. An instability index related to the vertical gradient of the moist static energy is found to be useful for depicting the onset of MJO convection along the equator. During warm events, the stronger magnitudes of this index over the central Pacific are conducive to more eastward penetration of convective anomalies in the region. These changes are mainly due to the intensified moisture accumulation at low levels. Analysis of the moisture budget suggests that the stronger moisture accumulation can be related to the increased low-level humidity over the central Pacific during warm events.

1. Introduction

Being the dominant mode of intraseasonal variability in tropical regions, the Madden-Julian Oscillation (MJO) remains to be a topic of intensive research in tropical meteorology since its discovery three decades ago (Madden and Julian 1971, 1972, 1994). Signals of the MJO are discernible in a number of meteorological variables, such as the upper- and low-level zonal wind and sea-level pressure. The perturbations of these fields associated with the MJO are characterized by large-scale, eastward propagating features. Based on outgoing longwave radiation (OLR) data, Lau and Chan (1985) showed that the MJO affects convective

Corresponding author and present affiliation: Chi-Yung Tam, International Pacific Research Center (IPRC), School of Ocean and Earth Science and Technology (SOEST), University of Hawai at Manoa, 1680 East West Road, Post Bldg., Honolulu, Hl 96822, Hawai

activity over the Indian Ocean and the western Pacific. The stronger intraseasonal convective features in the Eastern Hemisphere, and the relatively weaker signals in the Western Hemisphere, have been noted by Salby and Hendon (1994). The importance of the MJO in the tropical climate is further highlighted by its impact on the Indian and Australian summer monsoon (Lau and Chan 1986; Hendon and Liebmann 1990), and its influence on phenomena with shorter timescales such as tropical cyclones (Maloney and Hartmann 2000). The extratropical circulation is also linked to MJO activity (Weickmann et al. 1985; Knutson and Weickmann 1987), but the effects are less significant than those in the Tropics.

Recently it has become clear that the MJO also exhibits considerable interannual variability (Hendon et al. 1999; Slingo et al. 1999). Since ENSO is a major contributor to climate variability in the Tropics, it is natural to study its relationship with the MJO. Gutzler (1991) examined the intraseasonal variance of the 200 and 850 mb zonal wind using station data. In the December–February season during El Niño events, enhanced (suppressed) activity of the intraseasonal 850 mb zonal wind was found east (west) of the dateline. Using OLR data, Anyamba and Weare (1995) reported that during two out of the three warm ENSO events considered, there was more eastward penetration of intraseasonal activity or the MJO envelope over the central Pacific, and the propagation speed is slower. Later studies using OLR data with a longer base period (Fink and Speth 1997; Vincent et al. 1998; Hendon et al. 1999; Kessler 2001) came to similar conclusions. This east-west dipole-like perturbation of activity is reversed during cold ENSO events. The above observational results suggest that there is a positive correlation between MJO activity and the warmer underlying SST near the central Pacific.

Slingo et al. (1999) made use of the output of an ensemble experiment to study the relationship between SST forcing and the MJO. However, they noted that the observed year-to-year variation of the amount of overall MJO activity was not reproduced in the model atmosphere. Based on a global measure of the MJO amplitude (namely the zonal mean of the 200 mb zonal wind at the equator), their model results indicated that the internal variability of the MJO is much stronger than the perturbations caused by the changing SST conditions. Hendon et al. (1999) arrived at similar conclusions concerning the interannual variability of the MJO and the impact of the SST forcing, based on observational data for the zonal wind and OLR.

While the overall MJO activity in the Tropics seems to be weakly related to the SST conditions, the local behavior of the MJO could still be sensitive to the phase of ENSO. The modulation of the MJO in different geographical regions is an interesting issue in its own right. Delineating the local relationship between ENSO and MJO also contributes to a more comprehensive understanding of the ENSO influences on the atmospheric circulation. The goal of this study is to address this problem using both reanalysis data and output from an atmospheric GCM which is capable of producing a high level of MJO activity, as has been demonstrated in the analyses by Hendon (2000) of simulations from the same model.

It should be mentioned that in our GCM experiment SST conditions over the central to eastern Pacific are prescribed, and there is no response of the ocean to atmospheric activity. It has been suggested that the MJO might play a role on the onset of El Niño events (Kessler and McPhaden 1995; Kessler and Kleeman 2000). It is beyond the scope of this study to investigate the full interaction between the MJO and ENSO in a model environment. This would require the use of atmosphere-ocean coupled GCMs. Also, our model setup means that any impact on the MJO due to ENSO-related changes of the Indian Ocean SST is not simulated. Nevertheless, to the extent that the east-west shift of intraseasonal activity near the central Pacific is controlled by the underlying SST conditions (see discussion of Kessler 2001), results from the numerical experiment should shed light on how ENSO affects the MJO in the western-central Pacific region.

The present paper is organized as follows. In Section 2, the GCM and the experimental setup, as well the observational dataset, are described. The impact of ENSO on the local amplitude, propagation and growth/decay patterns of the MJO is the subject of Section 3. Using GCM data, detailed evolution of the cir-

culation and convection during the MJO lifecycle, and the possible role played by the SST conditions during warm and cold ENSO episodes, are considered in Section 4. The influences of various processes on the vertical profile of moist static energy, and the implications on MJO activity over the central equatorial Pacific are examined in Section 5. Discussion and summary of findings are given in Section 6.

2. Description of datasets

a. The GCM experiment

In this study, the output from a numerical experiment using the Geophysical Fluid Dynamics Laboratory (GFDL) climate GCM is analyzed. The GCM has a rhomboidal truncation at 30 wavenumbers which corresponds to a resolution of 3.75° (longitude) × ~2.2° (latitude) at the Equator, and has 14 unevenly spaced sigma levels. Physical processes such as radiative transfer, ground hydrology and gravity-wave drag are included. The clouds in the model atmosphere are predicted, and convection is parameterized using the moist convective adjustment scheme of Manabe et al. (1965). Bulk aerodynamic formulas are used for surface wind stress, sensible heat flux and evaporation. More detailed descriptions of the model are given by Gordon and Stern (1982) and Broccoli and Manabe (1992).

The GCM experiment is described by Lau and Nath (2003; see the description of their control experiment). This experiment was conducted with monthly-varying sea surface temperature (SST) prescribed within the deep tropical eastern Pacific (DTEP; 15°N–15°S, 172°E to the South American coast) from 1950 to 1999. Outside of DTEP, climatological SST was imposed. The experiment comprises eight runs, each being integrated for 50 years with the same sequence of boundary forcing, but initialized with different atmospheric conditions. Daily archived values are used in all analyses. Final results presented are based on ensemble averages over the eight individual integrations. All analyses are based on data for the November–March period.

b. Observational data

The observational dataset for this study is based on the products from the National Centers for Environmental Prediction (NCEP)-National Center for Atmospheric Research (NCAR) Reanalysis Project (Kalnay et al. 1996). In particular, it comprises the daily values of the upper-air winds, archived on a 2.5° × 2.5° lat-lon grid. Data from 1950 through 1999 are used. For ease of comparison with GCM results, all reanalysis data are interpolated on the same grid as that of the GCM.

3. Influences on the local amplitude, propagation and growth/decay of MJO

Before analyzing the modulations of the MJO by ENSO, the realism of the MJO in the model simulation was examined. For the same GCM dataset, Tam (2003) showed that the simulated zonal wind and large-scale divergent circulation have prominent wave-number one, eastward propagating signatures with a period of ~50 days. The variance map of the 25–100 day bandpass filtered[1] 850 mb zonal wind from the GCM simulation for all years (not shown) indicates strongest activity within the deep Tropics over the maritime continent and the western Pacific. The intraseasonal variance of the zonal wind for the GCM, averaged over an equatorial band from 40°E to 150°W, is about 30–40% larger than that given by reanalysis products (figures not shown). However, the MJO amplitude in the model atmosphere is relatively weak over the Indian Ocean, in contrast to observations which show comparable intraseasonal variability over the Indian Ocean and the western Pacific (see also Fig. 5 of Hendon 2000 for comparison between reanalysis data and simulation by the same GCM).

In order to study how ENSO affects MJO activity, the 25–100 day bandpass filtered variance of the 850 mb zonal wind during the November–March period is computed for each year. To remove the decadal-scale signals from the reanalysis data, an 11-year running mean, smoothed by a 1-2-1 filter, is first subtracted from the time series of the variance. The 50-year mean value of the original variance data is then added back to the resulting time series. This procedure is found to be effective in removing any long-term trends and inter-decadal fluctuations. Nine warm episodes and nine cold

1 In this study, bandpass filtering is achieved by using a 141-weight Lanczos filter.

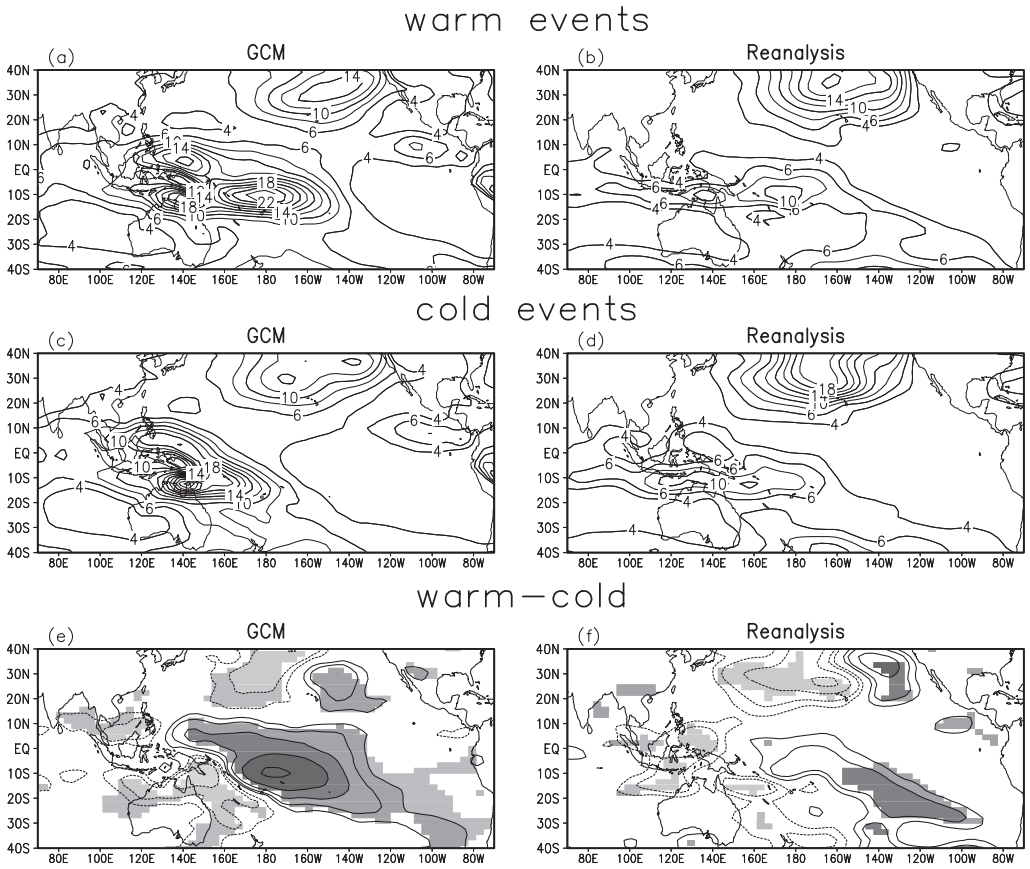

Fig. 1. Composites of the 25–100 day variance of the 850 mb zonal wind for (a,b) warm and (c,d) cold ENSO events for the November to March period. Contours start from 4 m^2s^{-2} with intervals of 2 m^2s^{-2}. (e,f) Differences between composites for warm and cold events. Computation is based on (a,c,e) GCM and (b,d,f) reanalysis data. Values of the difference between warm and cold composites exceeding the 95% (90%) significance level are shaded for the GCM (reanalysis) results. Dotted contours indicate negative values. Zero contours are omitted. Contour levels: (e) −4, −2, −1, 1, 2, 4, 8, and 16 m^2s^{-2}; (f) −6, −4, −2, −1, 1, 2, 4, and 6 m^2s^{-2}.

episodes in the period of 1950–99 are selected. The warm events chosen are: 1957–58, 1965–66, 1969–70, 1972–73, 1976–77, 1982–83, 1987–88, 1991–92 and 1997–98. The cold events are: 1950–51, 1954–55, 1955–56, 1964–65, 1970–71, 1973–74, 1975–76, 1988–89 and 1998–99. Figures 1a and 1c show the composites of the intraseasonal zonal wind variance based on GCM data for warm and cold events, respectively. Figures 1b and 1d give the warm and cold composites for the reanalysis data. As discussed above, the intraseasonal variability from the GCM is much stronger than that in the reanalyses. For the model simulation, the most striking feature is that strong activity is found farther eastward to the dateline during the warm ENSO events as compared to cold events. A similar change of the wind variance due to ENSO is also apparent in the reanalysis data, although it has a smaller magnitude. The differences between composites for warm and cold events are shown in Figs. 1e and 1f, based on GCM and reanalysis data respectively. Both maps show clearly that the ENSO-related modulation of the intraseasonal activity has a dipole pattern in the Tropics. In particular, during El Niño events there is stronger variance near and east of the dateline, and weaker variance over the maritime continent and the western Pacific. The reverse is true in La Niña

years[2]. The east-west shift of activity associated with the low-level zonal wind during ENSO is consistent with the results of Gutzler (1991) and Hendon et al. (1999, see their Fig. 9).

The above analyses indicate that enhanced intraseasonal activity of the 850 mb zonal wind over the central Pacific is found in the warm ENSO phase, whereas in the cold phase activity is stronger near its climatological maximum of variability over the maritime continent/western Pacific region. Inspection of the warm-minus-cold composite chart for the variance of the simulated precipitation (not shown) also reveals a dipole pattern similar to that associated with the low-level zonal wind. Activity is enhanced at the dateline and eastward, suppressed over northeastern Australia and New Guinea during warm events, while reversed changes occur during cold events. These ENSO impacts on the MJO circulation and convection will be considered in further detail in Section 4, by examining the evolution of these fields during the MJO lifecycle in warm and cold episodes.

To depict the local propagation characteristics and growth/decay rate of the MJO, a lag-correlation analysis is employed. This method has been used for studying the behavior of mid-latitude baroclinic waves (Blackmon et al. 1984; Wallace et al. 1988), and tropical synoptic-scale disturbances (Lau and Lau 1990). Using the 25–100 day bandpass filtered velocity potential[3] (χ), 8-day-forward and 8-day-backward lag correlation maps for a given reference point is computed. Based on these correlation maps, the phase speed of the MJO at that grid point is estimated by measuring the distance between the locations for the maximum forward and backward lag correlation signal, and dividing it by the total time lag (i.e., 16 days). The orientation of the phase velocity vector is parallel to the line joining these two maxima. Local growth rate of the anomalies is obtained by computing the difference between the values of the forward and backward regression, as evaluated at the aforementioned grid points that give maximum correlation, and dividing it by the total time lag.

The propagation and growth of MJO signals at various locations can be found by applying the above procedure at every grid point. Figures 2a–2b show the results based on the GCM 200 mb χ field, separately for warm and cold events. Both plots show prevalent eastward propagation of the anomalies; meridional movement is much smaller. Strong growth exists over the Indian Ocean, while decay of MJO signals occurs east of the maritime continent.

The most striking difference between warm and cold events is the eastward shift in Fig. 2a of about 20°–30° of the growth/decay couplet over a broad region from the Indian Ocean to the Pacific. During warm events MJO anomalies amplify strongly until they reach ~130°E, and then decay in regions farther east. During cold events, growth of anomalies is also found over the Indian Ocean, but they begin to decay east of ~100°E.

Based on this lag correlation technique, the climatological value of the zonal phase speed of the MJO for both GCM and reanalyses (figures not shown) is about 8.5 and 11 ms^{-1} over the maritime continent and the eastern Pacific, respectively. It is found that ENSO also affects the propagation speed of the MJO. Figure 2c shows the warm-minus-cold composite of the MJO zonal phase speed based on GCM data. Zonal propagation is slowed down over the central and eastern Pacific by ~1 ms^{-1} in the warm phase as compared to the cold phase. The warm and cold ENSO composites for the moist stability in the model atmosphere, based on a definition analogous to that of Neelin and Held (1987), are also computed. Weaker moist stability over the central Pacific (not shown) is found during El Niño years, which might be conducive to the slower MJO propagation during warm events (see, e.g., Wang and Li 1994; Yu et al. 1998). Another possible mechanism for the change of the MJO phase speed is the advection by the time mean flow, as the mean upper-level zonal wind is decreased during warm ENSO events in the same central Pacific region in the November–March period (not shown). In fact, GCM results show that over

2 The same dipole pattern appears when climatological values of the variance are subtracted from the warm ENSO composites. Same for cold ENSO composites except there is a reversal of sign (figures not shown).

3 The velocity potential is chosen due to its emphasis on large-scale features, which is helpful for obtaining a smooth pattern for the propagation and growth of MJO signals.

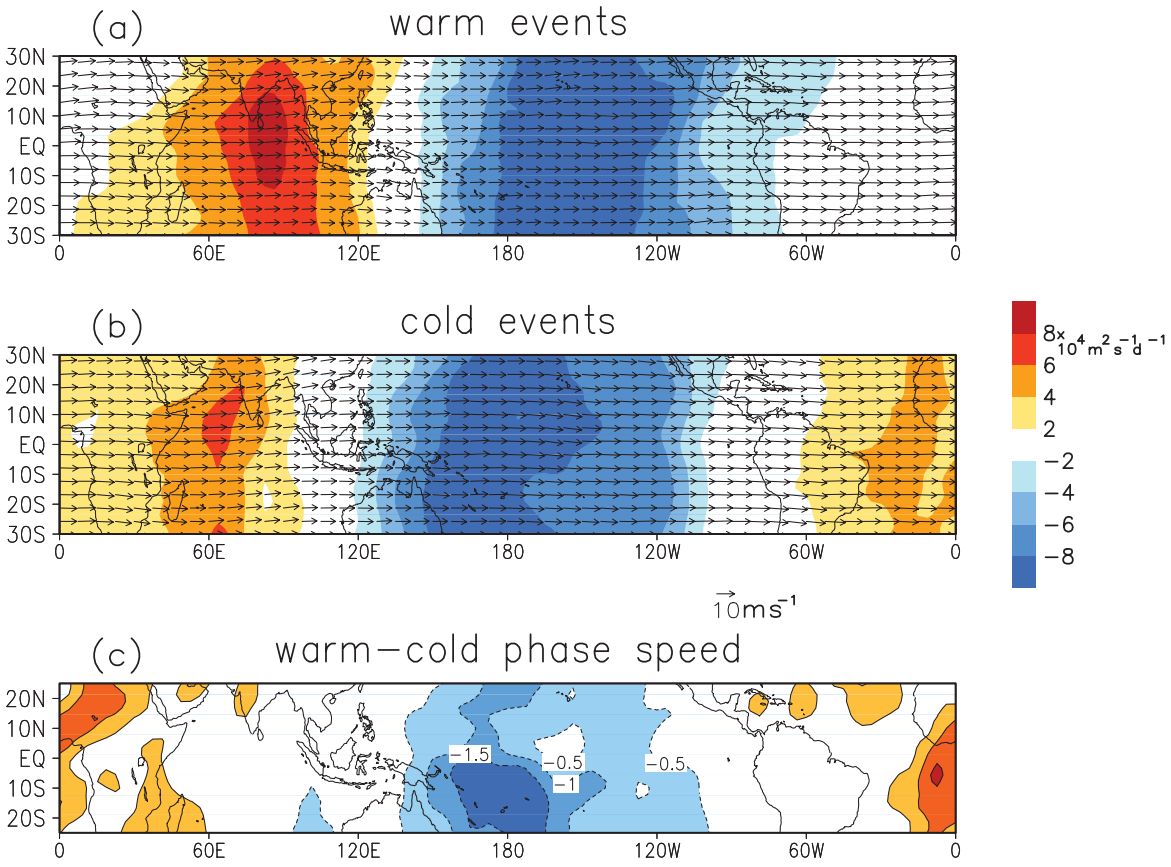

Fig. 2. Phase velocities (arrows; see scale at lower right of b) and growth rates (shading; see scale bar at right) of the 200 mb velocity potential for (a) warm and (b) cold ENSO events during the November–March period. Computation is based on GCM data. (c) Differences between warm and cold ENSO composites of the zonal phase speed, in units of ms^{-1}.

the equatorial Pacific the MJO phase speed is most positively correlated with the seasonal mean zonal wind at about 200 mb on interannual timescales. Further studies are needed to disentangle the effects of moist stability, and the structure of the time mean flow on the propagation of the MJO.

The corresponding results for reanalysis data are shown in Fig. 3. Only ENSO events within the period of 1979–1999 are selected for constructing these composite maps. Since the velocity potential is determined by the divergent part of the circulation, data before the satellite era (i.e., pre-1979 data) are not used. The overall growth/decay pattern is located more to the west, compared with the GCM results. Due to the smaller size of the reanalysis dataset, the results in Fig. 3 are noisier than the model patterns, and the detailed meridional structure of the growth might not be significant. The reanalyses agree with the GCM in showing an eastward shift of the growth/decay pattern in the warm phase, and such shift relative to the cold phase seems even more obvious than that seen in the model simulation[4]. The major effect of ENSO on the growth/decay pattern of the MJO is consistent with the previous result of an eastward shift of the region of strong intraseasonal activity during El Niño years (see Fig. 1). Also, the phase propagation of the MJO based on reanalysis data is found to be slower

4 For both model simulation and reanalyses, the growth/decay pattern is also shifted to the east (west) during warm (cold) events relative to the climatology.

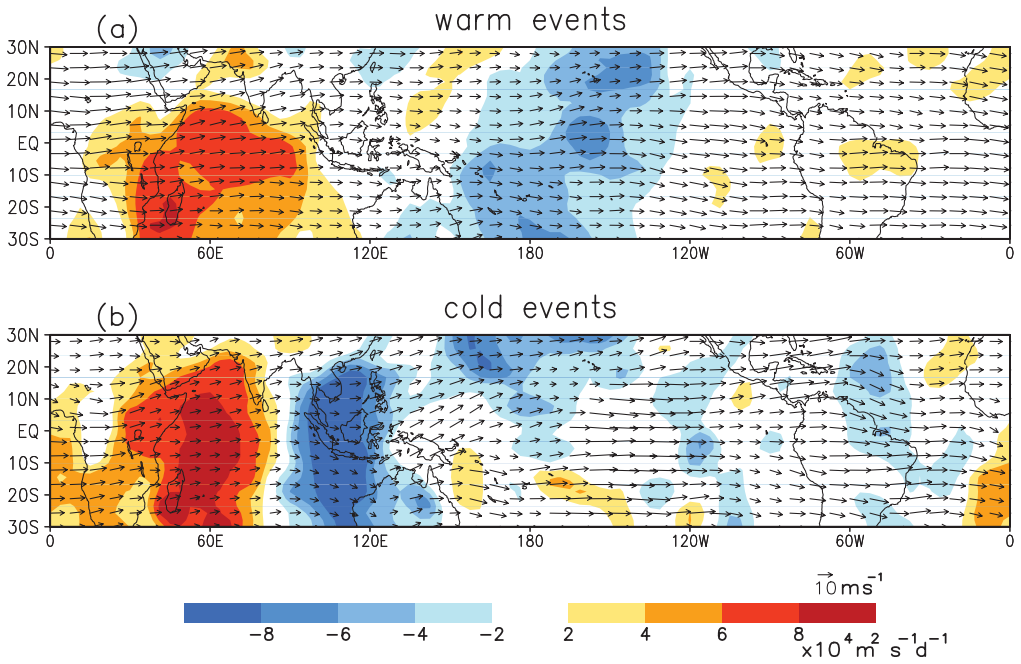

Fig. 3. As in Figs. 2a–2b, but for (a) warm ENSO events of 1982–83, 1987–88, 1991–92 and 1997–98 and (b) cold events of 1988–89 and 1998–99. Computation is based on reanalysis data.

during warm events (figure not show) as compared to its climatological values (for the base period of 1979–1999). The anomalous phase speed during El Niño events, averaged over the region of 130°E–130°W, 10°N–10°S, is about -0.8 ms^{-1}. The phase speed anomaly in the warm phase of ENSO for the GCM, averaged over the same region, is about -0.5 ms^{-1}.

In summary, ENSO is seen to influence the locations where strong activity occurs, growth/decay patterns and the propagation speed of the MJO. Such ENSO-related modulation on the MJO is found in the reanalysis dataset and simulated in the GCM experiment. In the next section, GCM data will be used to diagnose in detail the impact of ENSO on the evolution of the circulation and convection during the MJO lifecycle.

4. Circulation anomalies accompanying MJO evolution

In order to characterize the MJO cycle, the complex empirical orthogonal functions (CEOF) of the 10–100 day bandpass filtered 200 mb velocity potential are computed[5] (see, e.g., Horel 1984). Analyses are based on GCM data within the region of 20°N–20°S, for the period of November to March. The first CEOF accounts for more than 70% of the domain-integrated variance, and represents eastward propagating anomalies with a wavenumber-one structure (see Fig. B1 of Tam and Lau 2005). The evolution of the circulation and convection during the course of MJO are depicted by regressing the corresponding meteorological variables upon the real part of the standardized leading principal component (hereafter referred to as PC) time series. Regression maps are averaged over the lags of -12 to -9, -7 to -4 and -2 to 1 day. Figure 4 shows regression maps of the 850 mb streamfunction and precipitation, during warm and cold ENSO events[6]. These regression values give the typi-

5 Using the frequency band of 25–100 days for the CEOF analysis gives practically the same regression maps of circulation and convection.

6 Results for the warm and cold events are based on the same EOF (obtained from data for all years) in order to determine the phase of the MJO in a consistent manner. Essentially the same sequence of regression maps is found when EOFs are computed separately using data for warm and cold events.

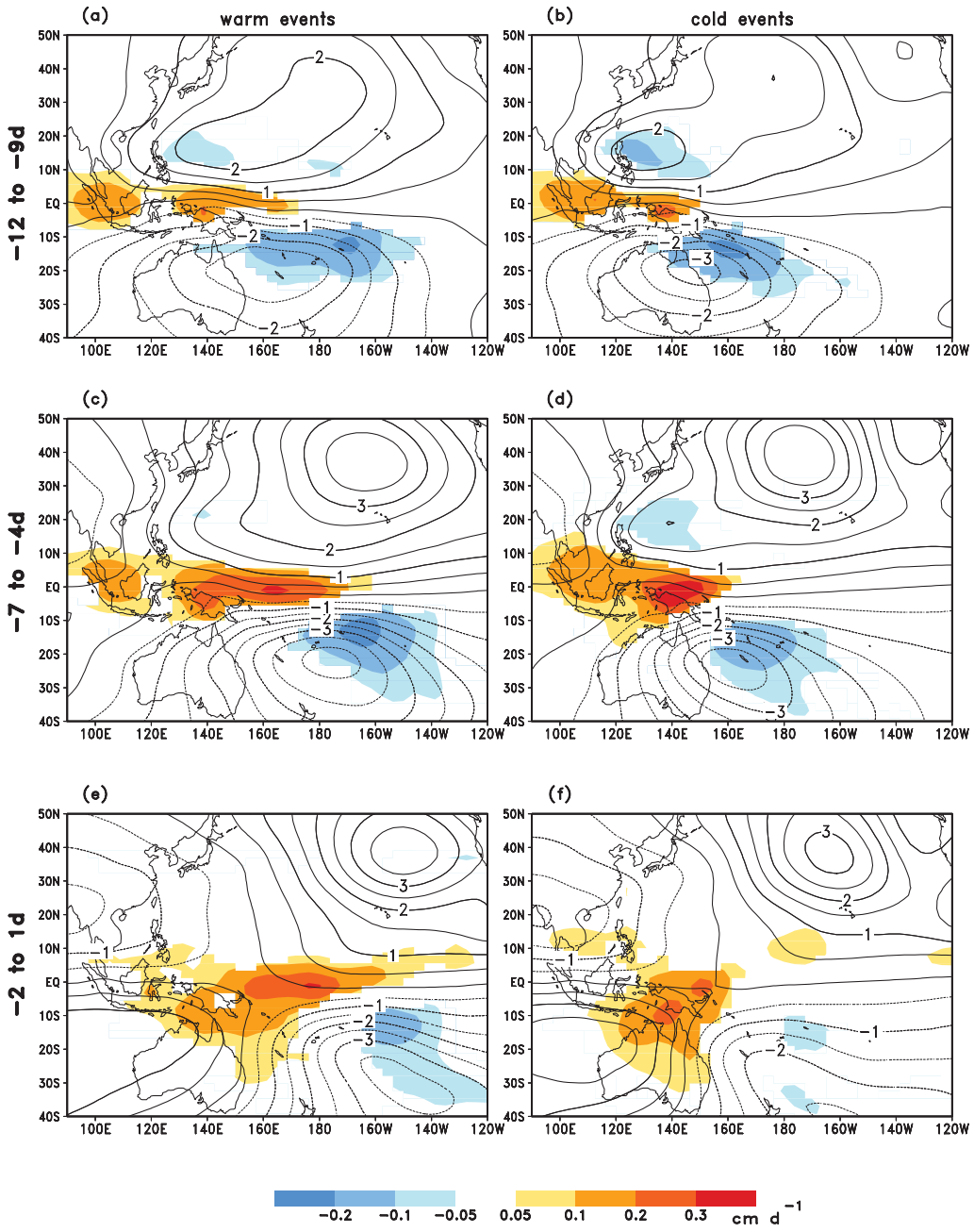

Fig. 4. Lag regression maps of GCM simulated precipitation (shading; see scale bar at bottom) and 850 mb streamfunction (contours; intervals: 5×10^4 $m^2 s^{-1}$) upon the real part of the PC of the leading CEOF of the 200 mb velocity potential. Regression maps are averaged over the neighboring lags of (a,b) −12 to −9 days; (c,d) −7 to −4 days; and (e,f) −2 to 1 day, and are based on data for the (a,c,e) warm and (b,d,f) cold ENSO events. All precipitation signals shown in this figure exceed the 95% significance level.

cal amplitudes for one standard deviation change of the PC time series. From both sequences of charts, positive precipitation anomalies are seen to propagate eastward into the western Pacific. There is also growth and then decay of the amplitudes of convective signals across the three time frames. The three lag periods will be referred to as the onset (i.e., day −12 to day −9), mature (day −7 to day −4) and decay stage (day −2 to day 1) of the convection in the region. Circulation features such as the anticyclones in the both hemispheres also move to the east as time progresses. There are negative precipitation anomalies in off-equatorial locations (i.e., east of the Philippines and northeast of Australia), which can be traced back to perturbations at even earlier times at the Equator (not shown). It is noticed that the positive precipitation signals are largely coincident with easterly wind anomalies along the equator. This model feature is at variance with observations, which show that strong MJO convection tends to be found where the low-level wind is weak or even westerly (see, e.g., Hendon 2000). The evolution of the convective anomalies over the whole lifecycle (not shown) is generally similar to that presented by Knutson and Weickmann (1987). The observed convective anomalies over the Indian Ocean are at least as strong as those found in the western Pacific, whereas the GCM tends to produce stronger features in the Pacific region. Another difference is that the abrupt change in the sign of simulated precipitation anomalies located east to northeast of Australia (Figs. 4c–4d) is not seen in the composites of Knutson and Weickmann (1987; see their Fig. 9).

The most obvious difference between warm and cold events is that precipitation and circulation anomalies during warm events propagate all the way from the western into the central Pacific, with strong activity occurring in the vicinity of the dateline and even to its east. During cold events, disturbances tend to become quasi-stationary over the western Pacific in the mature and decay stages, with the strongest anomalous rainfall being located over New Guinea. The amplitude of precipitation anomalies in cold episodes decreases sharply east of 160°E. To ensure that these impacts due to ENSO are robust, precipitation data are also regressed upon the velocity potential at the location of 150°E, Equator. Results for the warm and cold events, such as the extent of the eastward propagation of signals, are consistent with those in Fig. 4 (figures not shown).

It is also noticed that within 120°–150°E, the MJO convective signals are actually *stronger* during cold events (see middle panels of Fig. 4). Inspection of 850 mb zonal wind composites (not shown) indicates that stronger anomalies in that field are also found in the same equatorial region during cold events. This is consistent with the fact that, over northern and northeastern Australia, streamfunction perturbations and its meridional gradient are stronger during cold events. The contrasts between warm and cold events are in accord with earlier results concerning the change of 850 mb zonal wind variance: enhanced (suppressed) activity over the central and eastern Pacific, and suppressed (enhanced) activity over a broad region in the western Pacific during the warm (cold) events.

5. Variation of moist static energy associated with MJO

Bladé and Hartmann (1993) suggested that pre-conditioning of the atmospheric structure is essential for the triggering of MJO convection. This pre-conditioning process can take the form of the accumulation of low-level moist static energy (h), which is defined as $C_pT + \phi + Lq$, where C_p is the heat capacity of air at constant pressure, T the temperature, ϕ the geopotential. L is the latent heat of vaporization, and q is the specific humidity. Kemball-Cook and Weare (2001; hereinafter referred to as KW) examined the onset of the MJO in off-equatorial sites. Based on radiosonde data, they showed that a slow increase of the low-level h, mainly due to moistening, precedes MJO convection. This is followed by a rapid drying of the atmosphere after the onset of convection. In order to further understand the relationship between the circulation and convection associated with the MJO, the evolution of h is examined here.

Figure 5 shows the Hovmoller diagrams of the anomalous precipitation and the 'instability index' Δh as averaged over 5°N to 5°S. The latter index is defined as $\Delta h = h(\sigma = 0.935) - h(\sigma = 0.46)$, and the values of h at the two sigma (σ) levels are computed as lag regression

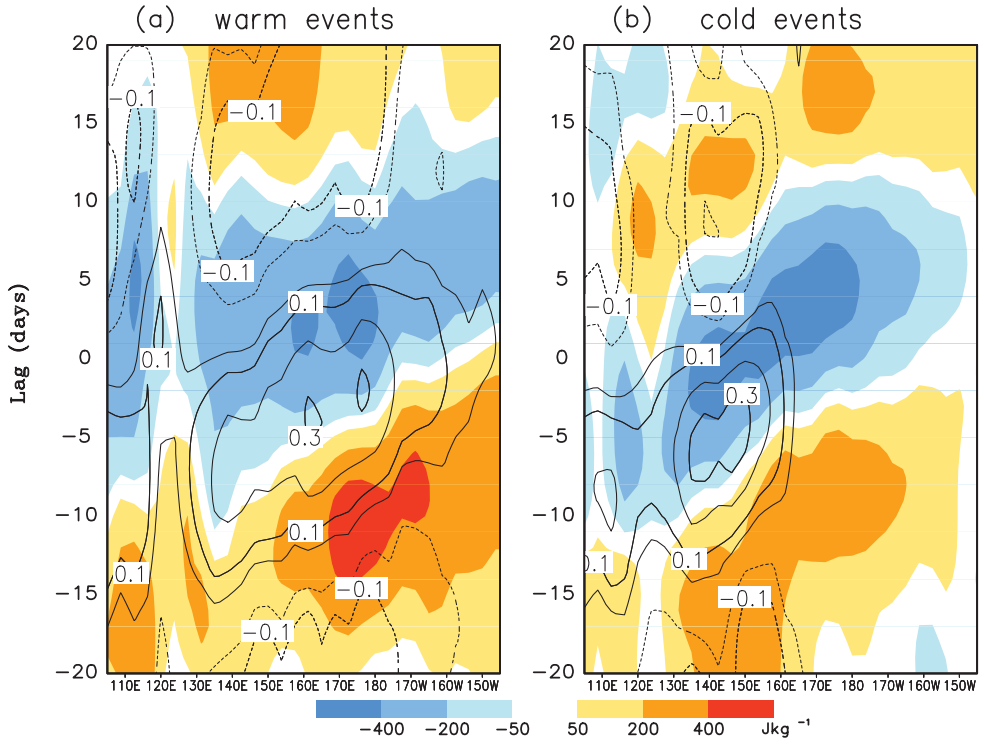

Fig. 5. Hovmoller diagrams for the lag regression, upon the real part of the leading PC of 200 mb velocity potential, of the moist static energy difference Δh (shading) between the levels $\sigma = 0.935$ and 0.46 and the precipitation (contours), during (a) warm and (b) cold ENSO events. Zero contours are omitted. Contour levels for precipitation: −0.2, −0.1, −0.05, 0.05, 0.1, 0.2 and 0.3 cm day^{-1}. Values are averaged over 5°N–5°S. Computation is based on the GCM dataset.

upon the real part of the PC of 200 mb velocity potential (see Section 4), based on GCM data. Δh is analogous to the instability index defined in KW, which is the difference of values of h at 1000 and 500 mb. For both warm and cold events, strong positive Δh precedes positive precipitation anomalies, with a lead of about 5 days. Furthermore, Δh changes sign when convection takes place and becomes negative when convection subsides and precipitation is suppressed. These relationships suggest that it is reasonable to treat Δh as an instability measure of the atmospheric column.

Consistent with the results in the last section, the precipitation anomalies shown in Fig. 5 penetrate farther eastward during warm events, with large amplitudes occurring in the vicinity of the dateline. Notice that the anomalies propagate eastward continuously in the warm ENSO phase, while in the cold phase they attain maximum amplitude at lag ≈ -5 days and the strongest signals do not propagate further[7]. It can be seen that ENSO also affects the evolution of Δh: there are much stronger positive Δh signals near the central Pacific at lag ≈ -12 days during the warm events as compared to the cold events. This finding is consistent with the interpretation that atmospheric pre-conditioning is necessary for MJO convection to occur. Failure to develop such a favorable environment could terminate the propagation of convective anomalies.

The vertical cross section of the regression values of h in different stages of the simulated MJO lifecycle is shown in Fig. 6, for both warm and cold events. Anomalies of Lq are also shown in each panel as contours. During the onset stage (Figs. 6a, 6d), h is largely controlled

7 During cold events, the positive Δh near the dateline is followed by very weak precipitation (<0.03 cm day^{-1}).

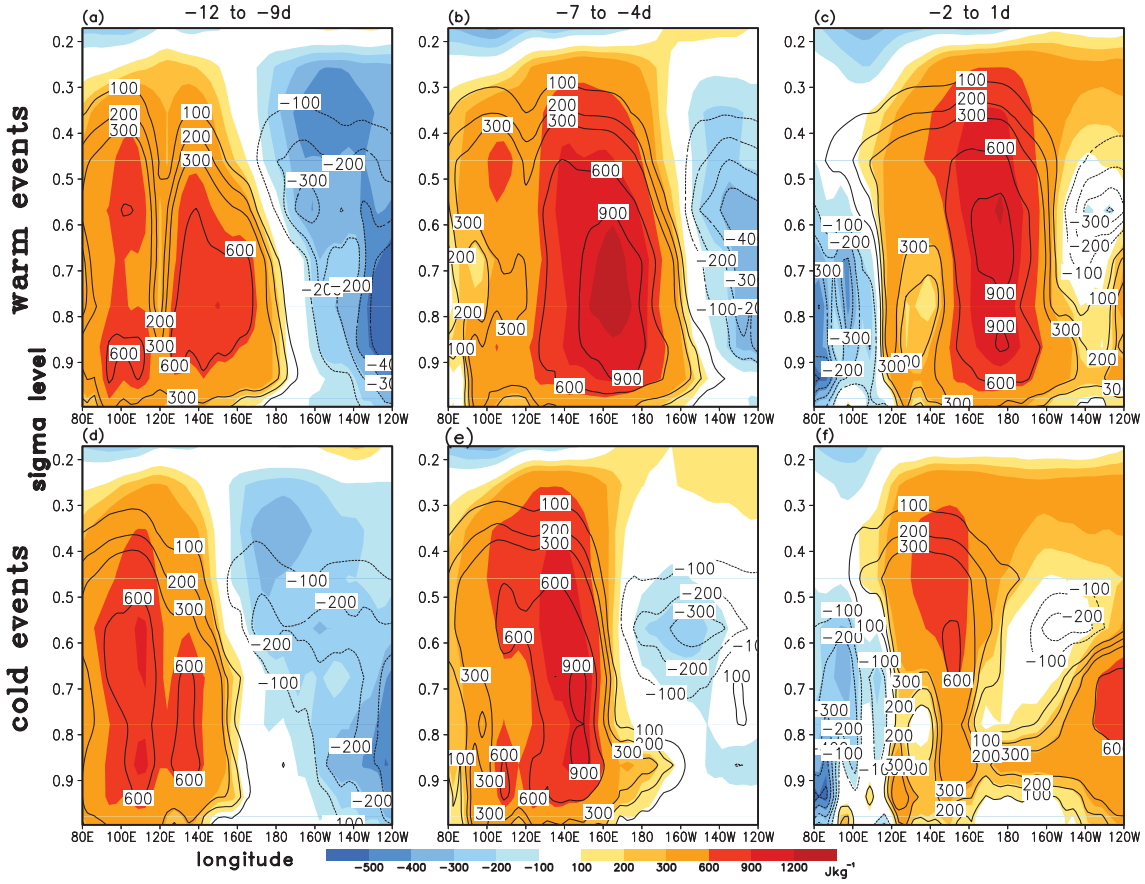

Fig. 6. Vertical cross sections of the lag regression of moist static energy h (shading; see scale bar at bottom) and specific humidity (multiplied by the latent heat of vaporization, contours) upon the real part of the leading PC of 200 mb velocity potential, averaged over 5°N–5°S. Regression values averaged over the neighboring lags of (a,d) −12 to −9 days, (b,e) −7 to −4 days and (c,f) −2 to 1 day. Upper and lower panels show results for warm and cold events, respectively. Zero contours are omitted. Contour levels for specific humidity: −400, −300, −200, −100, 100, 200, 300, 600 and 900 Jkg^{-1}. Computation is based on GCM simulations.

by the moisture anomalies. Over the western-central Pacific, considerable moistening of the low to middle troposphere has already occurred, leading to the positive values of Δh in Fig. 5 in this stage. It is noteworthy that stronger positive low-level moisture perturbations are found in the vicinity of the dateline during warm events. The stronger accumulation of the low-level q is mainly responsible for the larger Δh at about lag ≈ -12 days in the central Pacific during warm events, setting the stage for stronger convection there.

In the mature stage (Figs. 6b, 6e), h is distributed almost uniformly within the tropospheric column at about 150° to 160°E, and the vertical gradient of h is much reduced there. However, during warm ENSO episodes, there is still a substantial amount of h at the middle and low levels east of 170°E. This distribution suggests that convective anomalies would continue to develop in that region, and is consistent with the temporal development shown in Fig. 5. During the decay stage (Figs. 6c, 6f), the precipitation signals start to weaken, and Δh becomes negative.

Figure 7 shows the contribution to h from temperature anomalies (i.e., C_pT, see contours). Strong temperature anomalies are found in middle and upper levels. They attain large amplitudes during the mature stage of the con-

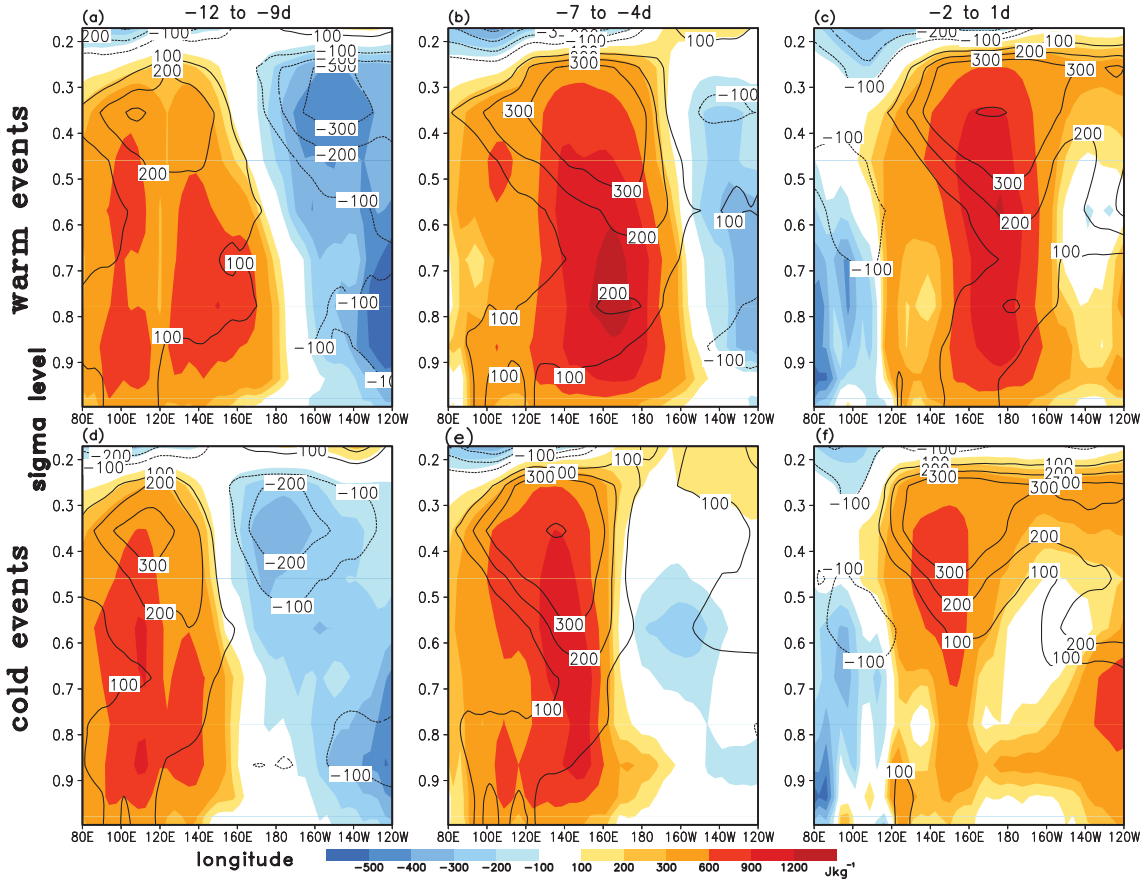

Fig. 7. As in Fig. 6, with the same shading patterns for h, but with contours depicting the lag regression of temperature (multiplied by the specific heat capacity of dry air at constant pressure).

vection. These large temperature perturbations tend to offset the effects of Lq, so that Δh is small in the mature stage. In the decay stage, the magnitude of moisture perturbations decreases in the lower troposphere (Fig. 6), while the temperature anomalies remain strong in the upper troposphere. As a result, Δh becomes negative. During warm events the temperature perturbations accompanying the enhanced convection signals in the western-central Pacific extend farther eastward.

To better understand the relationship between the anomalous circulation and moisture accumulation at low levels, the regression values of the 925 mb moisture tendency $\partial q/\partial t$, surface wind and surface pressure anomalies in the onset stage are plotted in Fig. 8. The convection peak is located at ~140°E (135°E) during warm (cold) ENSO events in this stage of the MJO lifecycle (see locations identified by the symbol P). In the vicinity and to the east of the strongest convection, surface pressure anomalies are negative and the zonal wind is directed down the pressure gradient. This pattern resembles the Gill-type response at low levels with heating located at the equator (Gill 1980). In off-equatorial regions to the east of the convection, there are strong meridional wind perturbations that are oriented down the local pressure gradient, thus leading to strong surface convergence along the Equator. This distinct cross-isobaric flow pattern in the vicinity of the convection center is indicative of the prominent role of frictional effects. Coincident with the surface convergence is the strong tendency of moisture aloft at 925 mb (shading in Fig. 8), suggesting that the vertical motion associated with the convergence could be responsible for the transport of moisture. Friction-induced low-level moisture accumulation east

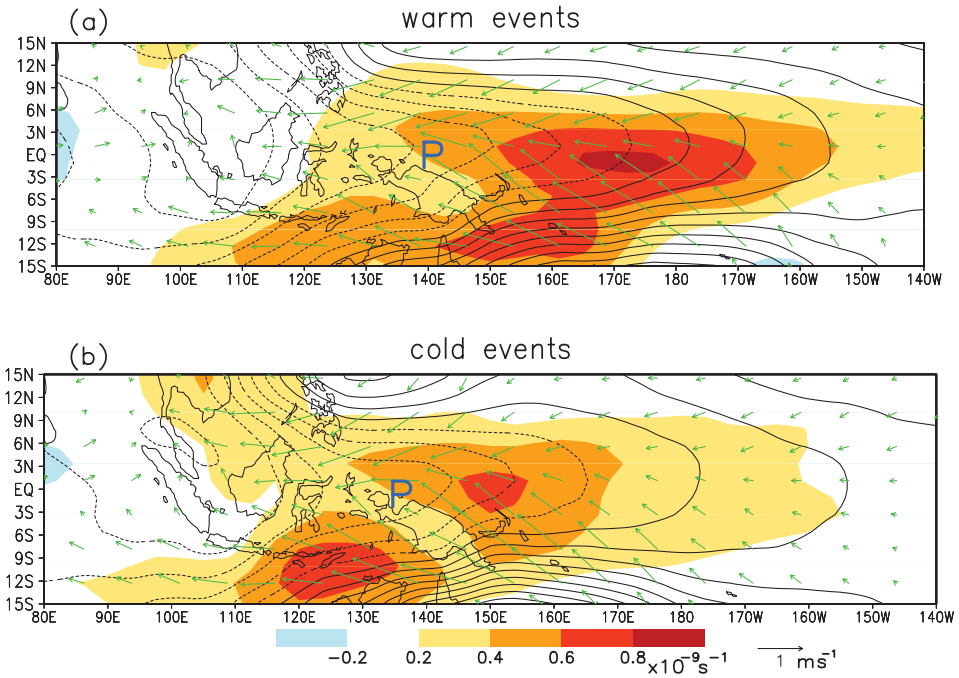

Fig. 8. Lag regression of the GCM simulated 925 mb moisture tendency $\partial q/\partial t$ (shading; see scale bar at bottom), surface wind (arrows; see scale at lower right) and surface pressure (contours; interval: 10 Pa; dotted contours indicate negative values) upon the real part of the leading PC of 200 mb velocity potential for (a) warm and (b) cold ENSO events. Regression maps are averaged over the lags of −12 to −9 days. The contemporaneous centers of convection are indicated by the symbol *P*.

of the peak MJO convection is also reported in the observational study of Maloney and Hartmann (1998). However, in the model atmosphere the convection center is too close to the maximum surface convergence to its east (collocated with the strongest moisture tendency in Fig. 8) as compared with the composites of Maloney and Hartmann (1998). During warm events, surface wind perturbations are stronger near 170°E, while those during cold events are confined to the far western Pacific. Associated with these different circulation features at the surface are the different locations of the strongest signals of $\partial q/\partial t$: strong moisture tendency during warm (cold) events extends more (less) to the east. The difference of $\partial q/\partial t$ signals is consistent with the low-level moisture perturbations in different phases of ENSO shown in Fig. 6.

The results in Figs. 6 and 8 suggest that low-level moistening due to moisture transport related to frictional convergence in the central Pacific has a strong effect on Δh, and could be crucial for the more eastward penetration of MJO convection during warm ENSO events. The processes for moisture accumulation and depletion are now considered in a more detailed manner. Figure 9 shows the equatorial cross section of moisture tendency as well as advection of mean moisture ($\bar{q}$) by the anomalous vertical motion ($\dot{\sigma} \equiv D\sigma/Dt$), i.e., $-\dot{\sigma}\partial_\sigma \bar{q}$, in the onset stage during warm and cold events. Examination of the MJO moisture budget (not shown) shows that, of the various budget terms, $-\dot{\sigma}\partial_\sigma \bar{q}$ is the main term that almost balances the moisture source or sink[8]. $\partial q/\partial t$ is usually much smaller and can be approximated by the difference between the vertical advection and source terms. Cross section of anomalous circulation as well as values of $\bar{q}$ are also shown to facilitate interpretation. For comparison,

8 In this phase of the MJO, the evaporation is negative over the maritime continent/western Pacific where the model has westerly mean wind at the surface. Its magnitude is ~1/5 to 1/10 of the column-integrated moisture advection.

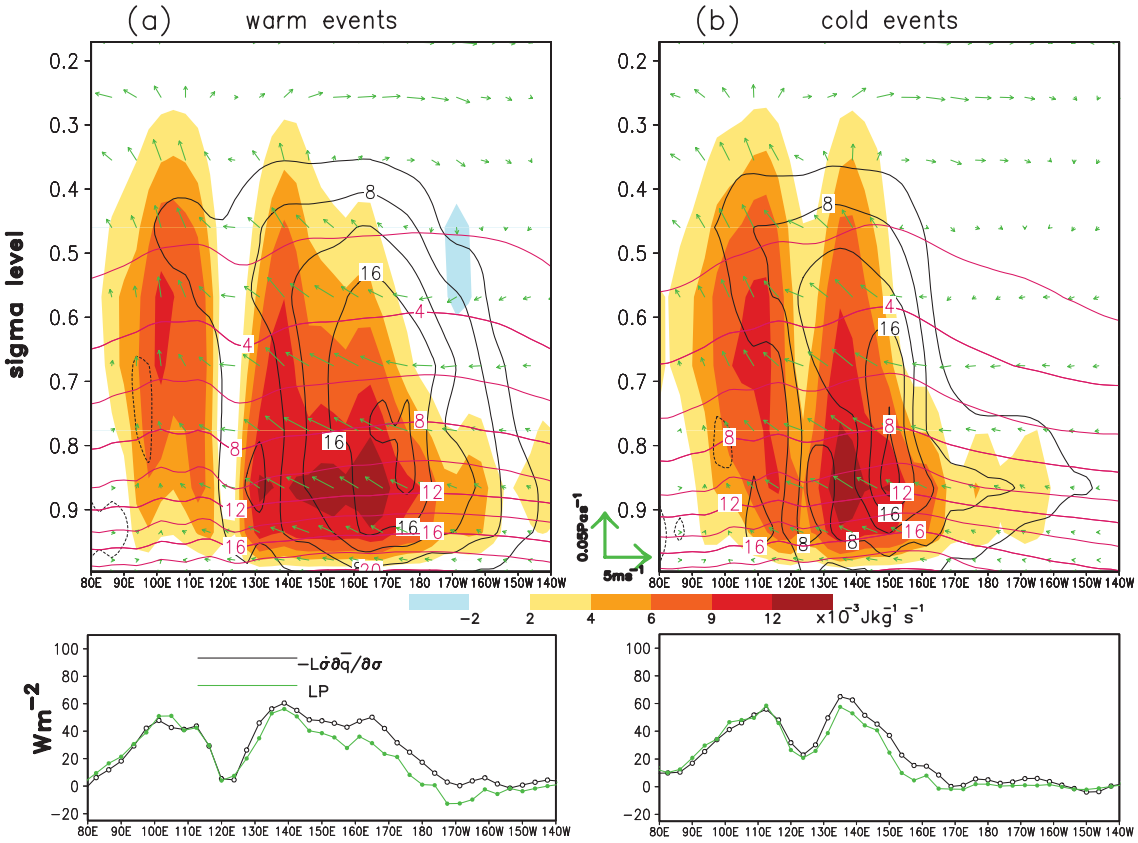

Fig. 9. Cross section of the vertical advection of moisture by anomalous circulation (shading; see scale bar under upper panels), zonal wind and pressure velocity (arrows, see scale between upper panels), and moisture tendency (black contours; interval: 4×10^{-4} Jkg^{-1}s^{-1}), averaged over 5°N–5°S. All results are based on regression values of GCM data upon the real part of the leading PC of 200 mb velocity potential, and are averaged over the lags of −12 to −9 days, for (a) warm and (b) cold events. The seasonal mean moisture (magenta contours; intervals: 2 g kg^{-1}) is also shown. Values of the column-integrated vertical advection (black curves) and precipitation (green curves) are shown in the lower panels, and have units of Wm^{-2}. All budget terms are multiplied by the latent heat of vaporization L.

column-integrated values of the vertical advection, and the precipitation field, are also displayed in the bottom panels.

Near the sites of maximum convective anomalies (the symbol *P* in Fig. 8), the vertical transport of moisture is strong with large values reaching the middle troposphere in the onset stage, while to the east of the peak convection the transport tends to be confined to low levels. It can be seen that there is a substantial amount of moisture advection east of ~170°E during warm events, while during cold events the vertical advection in the same region is much weaker. This contrast in the advection term can be attributed to differences in the magnitudes of $\dot{\sigma}$, and of the vertical gradient of the mean moisture $\partial_\sigma \bar{q}$ in the two phases of ENSO. In the warm phase $\dot{\sigma}$ is enhanced east of 150°E and the magnitude of $\partial_\sigma \bar{q}$ at the lowest levels is also increased (not shown). Rough estimates show that the difference of $\partial_\sigma \bar{q}$ between warm and cold events contributes ~20% to the difference of moisture advection at the lowest sigma levels near the dateline. The larger magnitude of $\partial_\sigma \bar{q}$ is due to the warmer SST in the central Pacific during El Niño events. The stronger perturbations of $\dot{\sigma}$ are associated with the stronger surface wind anomalies in the re-

gion east of 150°E during warm events (see Fig. 8), as the vertical motion at the lowest levels is tied to the friction-induced surface convergence at the Equator. (In the free atmosphere, convection probably plays a more important role.)

The bottom panels of Fig. 9 indicate that, to the east of the strongest convection, the column-integrated vertical advection (black curves) is larger than the precipitation (green curves) in both warm and cold phase of ENSO. Therefore, moisture is accumulated in the atmospheric column east of the strongest convective signals in the onset stage. However, in the region of 150°E to the east of the dateline, the difference between the column-integrated $-\dot{\sigma}\partial_\sigma\bar{q}$ and precipitation during warm events is noticeably greater than that during cold events. This larger difference between the two budget terms thus leads to more accumulation of moisture during warm events as compared to cold events in the region.

The moisture budget terms in other stages of the MJO lifecycle are also considered. In the mature stage (not shown), when maximum precipitation occurs, strong vertical advection exists but is now mostly canceled by the moisture sink. It is found that during cold events, $\partial q/\partial t$ at low levels is weak or even negative, while during warm events accumulation of moisture is still present near the dateline. This is consistent with the evolution of the moisture perturbations during the lifecycle depicted in Fig. 6. Since low-level moisture perturbations is important in controlling Δh, these results suggest that the vertical gradient of the near-surface moisture field $\partial_\sigma\bar{q}$, which is closely related to the SST conditions, could play a substantial role in modulating the intensity of vertical moisture transport, and thereby affecting where strong MJO convection occurs. In the decay stage, $\partial q/\partial t$ is negative, with the magnitude of the advection term now being smaller than the moisture sink. Convection and vertical transport of moisture begin to subside, while as a whole the precipitation is depleting the atmospheric moisture.

6. Discussions and summary

Data from both reanalyses and a GCM experiment are used to study the ENSO-related variability of the MJO. It is demonstrated that the impact of ENSO on the intraseasonal oscillation is at least qualitatively captured in the GCM output. More detailed analysis of the GCM data suggests that the instability index introduced by KW can be useful for studying the onset of the MJO convection in equatorial regions and its interannual variation.

Results based on both datasets indicate that ENSO has a strong impact on MJO activity over the Pacific. During warm (cold) ENSO events, intraseasonal variance of the low-level zonal flow is enhanced (suppressed) over the central-eastern Pacific, and suppressed (enhanced) over the western Pacific. The growth/decay pattern associated with the MJO is found to be displaced eastward in the warm phase, as compared to the cold phase of ENSO. There is also evidence that the phase speed of the MJO over the equatorial Pacific is reduced during El Niño events.

For the GCM simulation, it is found that the instability index as measured by the vertical gradient of the anomalous moist static energy has stronger amplitudes over the central Pacific during warm ENSO events. MJO convection is able to propagate further eastward to the region. During cold events, smaller changes in this instability index are found and the convective anomalies stall in the western Pacific. Examination of the moisture budget reveals that vertical transport of moisture ahead of strong convection extends farther eastward to the dateline, during warm events as compared to cold events. Since the higher mean moisture content at low levels also contributes to the moisture tendency in the warm phase, it is suggested that the distribution of the mean moisture field could be important in determining the eastward extension of MJO convective signals during ENSO. The different low-level moisture content is ultimately related to the underlying SST conditions in different phases of ENSO.

The MJO in the model atmosphere is admittedly deficient in a number of aspects. Strongest convection is collocated with low-level easterlies, instead of weak or westerly wind anomalies, as found in observations. Hence, in the model the convection is too close to the frictional convergence signals (see Fig. 8). Results of Maloney and Hartmann (1998; their Fig. 10) indicate that surface convergence is about 60° east of the convection. Neverthe-

less, the GCM does replicate an analogous mechanism of low-level moistening, which is important for sustaining the MJO signals in this model. We expect that during ENSO when the SST conditions are perturbed, processes controlling the MJO propagation similar to those in simulation (see previous paragraph) also operate in the real atmosphere. Finally, it is possible that other processes (such as those related to the maintenance of the MJO; see, e.g., Grabowski 2003) also play a role in this problem.

The influence of ENSO on the intraseasonal convective signals could affect the intraseasonal variability in the extratropical Pacific. For instance, during cold events there are stronger and more stationary precipitation anomalies in the far-western Pacific. This variation of tropical condensational heating could change the forcing of the low-frequency circulation in the extratropical Pacific (Barsugli and Sardeshmukh 2002). In fact the MJO-related extratropical wavetrain in the model atmosphere is greatly affected by ENSO. Tam and Lau (2005) discussed this effect of the interannual variability of the MJO on the circulation over the North Pacific.

Acknowledgments

We would like to thank Isaac Held and Paul Kushner for their interest and encouragement throughout the course of this study. John Lanzante has conducted the GCM integration used in this study, and has shared with us his program codes for performing CEOF analyses.

References

Anyamba, E.K. and B.C. Weare, 1995: Temporal variability of the 40–50-day oscillation in tropical convection. *Int. J. Climatol.*, **15**, 379–402.

Barsugli, J.J. and P.D. Sardeshmukh, 2002: Global atmospheric sensitivity to tropical SST anomalies throughout the Indo-Pacific basin. *J. Climate*, **15**, 3427–3442.

Blackmon, M.L., Y.-H. Lee, J.M. Wallace, and H.-H. Hsu, 1984: Time variation of 500 mb height fluctuations with long, intermediate and short time scales as deduced from lag-correlation statistics. *J. Atmos. Sci.*, **41**, 981–991.

Bladé, I. and D.L. Hartmann, 1993: Tropical intraseasonal oscillations in a simple nonlinear model. *J. Atmos. Sci.*, **50**, 2922–2939.

Broccoli, A.J. and S. Manabe, 1992: The effects of orography on midlatitude northern hemisphere dry climates. *J. Climate*, **5**, 1181–1201.

Fink, A. and P. Speth, 1997: Some potential forcing mechanisms of the year-to-year variability of the tropical convection and its intraseasonal (25–70-day) variability. *Int. J. Climatol.*, **17**, 1513–1534.

Gill, A.E., 1980: Some simple solutions for heat-induced tropical circulation. *Quart. J. Roy. Meteor. Soc.*, **106**, 447–462.

Gordon, C.T. and W.F. Stern, 1982: A description of the GFDL global spectral model. *Mon. Wea. Rev.*, **110**, 625–644.

Grabowski, W.W., 2003: MJO-like coherent structures: Sensitivity simulations using the Cloud-Resolving Convection Parameterization (CRCP). *J. Atmos. Sci.*, **60**, 847–864.

Gutzler, D.S., 1991: Interannual fluctuations of intraseasonal variance of near-equatorial zonal winds. *J. Geophys. Res.*, **96**, 3173–3185.

Hendon, H.H., 2000: Impact of air-sea coupling on the Madden-Julian oscillation in a general circulation model. *J. Atmos. Sci.*, **57**, 3939–3952.

——— and B. Liebmann, 1990: A composite study of onset of the Australian summer monsoon. *J. Atmos. Sci.*, **47**, 2227–2240.

———, C. Zhang, and J.D. Glick, 1999: Interannual variation of the Madden-Julian oscillation during austral summer. *J. Climate*, **12**, 2538–2550.

Horel, J.D., 1984: Complex principal component analysis: Theory and examples. *J. Appl. Meteor.*, **23**, 1660–1673.

Kalnay, E. and Coauthors, 1996: The NCEP/NCAR 40-year reanalysis project. *Bull. Amer. Meteor. Soc.*, **77**, 437–471.

Kemball-Cook, S.R. and B.C. Weare, 2001: The onset of convection in the Madden-Julian oscillation. *J. Climate*, **14**, 780–792.

Kessler, W.S., 2001: EOF representations of the Madden-Julian oscillation and its connection with ENSO. *J. Climate*, **14**, 3055–3061.

——— and R. Kleeman. 2000: Rectification of the Madden-Julian oscillation into the ENSO cycle. *J. Climate*, **13**, 3560–3575.

——— and M.J. McPhaden, 1995: Oceanic equatorial waves and the 1991–93 El Niño. *J. Climate*, **8**, 1757–1776.

Knutson, T.R. and K.M. Weickmann, 1987: 30–60 day atmospheric oscillations: Composite life cycles of convection and circulation anomalies. *Mon. Wea. Rev.*, **115**, 1407–1436.

Lau, K.-H. and N.-C. Lau, 1990: Observed structure and propagation characteristics of tropical summertime synoptic scale disturbances. *Mon. Wea. Rev.*, **118**, 1888–1913.

Lau, K.-M. and P.H. Chan, 1985: Aspects of the 40–

50 day oscillation during the northern winter as inferred from outgoing longwave radiation. *Mon. Wea. Rev.*, **113**, 1889–1909.

——— and ———, 1986: Aspects of the 40–50 day oscillation during the northern summer as inferred from outgoing longwave radiation. *Mon. Wea. Rev.*, **114**, 1354–1367.

Lau, N.-C. and M.J. Nath, 2003: Atmosphere-ocean variations in the Indo-Pacific sector during ENSO episodes. *J. Climate*, **16**, 3–20.

Madden, R.A. and P.R. Julian, 1971: Detection of a 40–50 day oscillation in the zonal wind in the tropical Pacific. *J. Atmos. Sci.*, **28**, 702–708.

——— and ———, 1972: Description of global-scale circulation cells in the tropics with a 40–50 day period. *J. Atmos. Sci.*, **29**, 1109–1123.

——— and ———, 1994: Observations of the 40–50-day tropical oscillation—a review. *Mon. Wea. Rev.*, **122**, 814–837.

Maloney, E.D. and D.L. Hartmann, 1998: Frictional moisture convergence in a composite life cycle of the Madden-Julian oscillation. *J. Climate*, **11**, 2387–2403.

——— and ———, 2001: The Madden-Julian oscillation, barotropic dynamics, and North Pacific tropical cyclone formation. Part I: Observations. *J. Atmos. Sci.*, **58**, 2545–2558.

Manabe, S., J. Smagorinsky, and R.F. Strickler, 1965: Simulated climatology of a general circulation model with a hydrological cycle. *Mon. Wea. Rev.*, **93**, 769–798.

Neelin, J.D. and I.M. Held, 1987: Modeling tropical convergence based on the moist static energy budget. *Mon. Wea. Rev.*, **115**, 3–12.

Salby, M.L. and H.H. Hendon, 1994: Intraseasonal behavior of clouds, temperature, and motion in the tropics. *J. Atmos. Sci.*, **51**, 2207–2224.

Slingo, J.M., D.P. Rowell, K.R. Sperber, and F. Nortley, 1999: On the predictability of the interannual behaviour of the Madden-Julian oscillation and its relationship with El Niño. *Quart. J. Roy. Meteor. Soc.*, **125**, 583–609.

Tam, C.-Y., 2003: The impact of ENSO on tropical and extratropical atmospheric variability on intraseasonal and synoptic time scales as inferred from observations and GCM simulations. Ph.D. dissertation, Princeton Univ., New Jersey, 197 pp.

Tam, C.-Y. and N.-C. Lau, 2005: The impact of ENSO on atmospheric intraseasonal variability as inferred from observations and GCM simulations. *J. Climate*, **18**, 1902–1924.

Vincent, D.G., A. Fink, J.M. Schrage, and P. Speth, 1998: High- and low-frequency intraseasonal variance of OLR on annual and ENSO timescales. *J. Climate*, **11**, 968–986.

Wallace, J.M., G.-H. Lim, and M.L. Blackmon, 1988: Relationship between cyclone tracks, anticyclone tracks and baroclinic waveguides. *J. Atmos. Sci.*, **45**, 439–462.

Wang, B. and T. Li, 1994: Convective interaction with boundary-layer dynamics in the development of a tropical intraseasonal system. *J. Atmos. Sci.*, **51**, 1386–1400.

Weickmann, K.M., G.R. Lussky, and J.E. Kutzbach, 1985: Intraseasonal (30–60 day) fluctuations of outgoing longwave radiation and 250 mb streamfunction during northern winter. *Mon. Wea. Rev.*, **113**, 941–961.

Yu, J.-Y., C. Chou, and J.D. Neelin, 1998: Estimating the gross moist stability of the tropical atmosphere. *J. Atmos. Sci.*, **55**, 1354–1372.